Vibronic coupling in C$_2$H: implications for astrochemistry

Benjamin A. Laws,[*,†,‡] Zachariah D. Levey,[†] John F. Stanton,[¶]

Timothy W. Schmidt,[†] and Stephen T. Gibson[‡]

†School of Chemistry, University of New South Wales, Sydney NSW 2052, Australia

‡Research School of Physics, The Australian National University, Canberra ACT 2601, Australia

¶Department of Chemistry, University of Florida, Gainesville, Florida 32611, United States

E-mail: b.laws@unsw.edu.au

Abstract

Introduction

Carbon monohydrides $C_{2n}H$, are a class of linear radicals that play an important role in combustion and interstellar chemistry. These carbon chains have been observed in many interstellar environments, including planetary atmospheres, comets, dark clouds, and during heavy star formation. Due to their relatively high abundance in a variety of astronomical conditions, they are believed to be promising candidates for Diffuse Interstellar Band (DIB) carriers. The corresponding anions $C_{2n}H^-$ are also believed to play an important role in interstellar chemistry. C_6H^- was the first negative ion detected in space, after it was observed in two distinct interstellar molecular clouds IRC+10216 and TMC-1 in 2006. More recently, anions C_4H^- and C_8H^- have also been detected in a range of environments, include dark clouds, prestellar cores, and prostellar envelopes.

Chain growth of the $C_{2n}H$ radicals occurs predominately through acetylene addition,

$$C_{2n}H + C_2H_2 \rightarrow C_{2n+2}H + H_2. \tag{1}$$
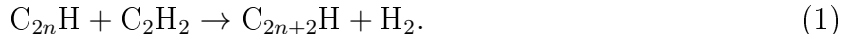
Conversely, the formation of anions in space is believed to be driven by radiative electron attachment, charge transfer, and dissociate electron attachment. Current astrochemical modelling of interstellar clouds, such as IRC+1026, typically underestimate the observed abundances of CH_4^-. Therefore, it has been proposed that ion-neutral reactions

$$C_{2n}H^- + C_2H_2 \rightarrow C_{2n+2}H^- + H_2. \tag{2}$$

may be significant chain growth mechanisms that also needs to be included. Modelling of the extraterrestrial planetary atmosphere of Saturn's moon Titan, suggests that both C_2H

and C_2H^- play an important role in the atmospheric chemistry. Multiple reaction pathways were included for the ion C_2H^- including reactions with C_2H_2 and HCN.

Understanding interstellar chemistry relies critically on theory, to provide a link between astronomical observations and terrestrial laboratory studies. Microwave spectroscopy has successfully been used in this fashion to identify a large number of molecules in the interstellar medium (ISM). However for some species, particularly those with low abundances or no dipole moment, UV/vis spectroscopic methods are required for identification. This creates a challenge for theory, as electronic spectra calculations are more sensitive to the level of theory employed than pure rotational spectra. This becomes even more challenging when vibronic coupling effects are introduced, as they can be exceedingly difficult to model.

These considerations may be explored by examining some of the smallest carbon mono-hydrides. The ethynyl radical C_2H may appear to be a simple linear triatomic molecule. However the electronic spectrum is complicated by the presence of the close-lying ground $^2\Sigma^+$ and first excited $^2\Pi$ surfaces, which are only separated by $\sim 3,600$ cm^{-1}. The interaction of these surfaces produces a complex vibronic spectrum around the $\tilde{A}^2\Pi$ state, where the $\tilde{X} - \tilde{A}$ origin is spread over multiple admixed vibronic levels. In C_4H the $^2\Sigma^+$ and $^2\Pi$ states are nearly degenerate, resulting in even stronger coupling, while in C_6H and C_8H the ordering of the states swaps, with a ground $^2\Pi$ state and a low lying excited $^2\Sigma^+$ state. Consequently, understanding these vibronic coupling interactions between the $^2\Sigma$ and $^2\Pi$ surfaces will be essential in order to accurately model the role these radicals (and their corresponding anions) are likely to play in the interstellar chemistry mentioned above, and to guide the search for possible DIB carriers.

In this paper we study the vibronic spectrum of the ethynyl radical C_2H by employing High-Resolution Photoelectron Imaging (HR-PEI) in order to benchmark CFOUR *ab-initio* vibronic-coupling calculations. C_2H is reported to be one of the most abundant molecules in the universe, and is the most thoroughly studied of the $C_{2n}H$ species. Many different experimental techniques have been employed to try and resolve the complex vibronic spec-

trum, including electron spin resonance, laser magnetic resonance, microwave and milli-meter wave spectroscopy, infrared (matrix isolation and Fourier Transform) spectroscopy, and photoelectron spectroscopy. C_2H has also received extensive theoretical attention to try and understand the experimental results, however the large number of possible vibronic levels means this has proven to be a challenge. In this work we demonstrate how construction of a quasiadiabatic Hamiltonian allows for the strength of vibronic interactions between coupled surfaces near a conical intersection to be calculated, in order to simulate electronic and vibronic spectra. By employing anion HR-PEI both the $^2\Sigma^+$ and $^2\Pi$ surfaces are mapped out on an equal footing from the anion $\tilde{X}^1\Sigma^+$ state, allowing for direct comparison to the *ab-initio* modelling.

Results and Analysis

Ethynyl ions were produced in a pulsed-jet discharge of pure C_2H_4 gas, and subsequently mass isolated via time of flight. Electrons were detached using a tuneable Sunlite Optical Parametric Oscillator (OPO) pumped with the third harmonic of a Nd:YAG laser. High electron counts could also be obtained by using the third and fourth harmonics of the Nd:YAG laser directly. The detached electrons were then mapped onto a micro channel plate detector using a Velocity Map Imaging (VMI) lens. An illustrative VMI of $\sim$4 million electrons collected from 355 nm (3.49 eV) photodetachment of C_2H^- is shown in Fig. 1(a). The electrons are distributed radially according to their speed, with slow electrons at the image center, and fast electrons located towards the outer edge. Due to the relatively large C_2H^- electron affinity (EA) of 2.969 eV,[1] photodetachment at 355 nm occurs close to threshold. This yields slow electrons, allowing for a low repeller voltage (-600 V) on the VMI lens, and high velocity resolution.

Despite being close to threshold, two electronic states of neutral C_2H are observed. The faster electrons on the outer edge correspond to $C_2H(\tilde{X}\,^2\Sigma^+) + e^- \leftarrow C_2H^-(\tilde{X}\,^1\Sigma^+) + h\nu$

photodetachment, and are preferentially distributed around the poles of the image, indica-tive of a positive anisotropy parameter. Conversely the angular distribution of the slower electrons near the center are skewed towards the equator, indicative of a negative anisotropy parameter. These electrons may be assigned to photodetachment to the first excited state $C_2H(\tilde{A}\,^2\Pi) + e^- \leftarrow C_2H^-(\tilde{X}\,^1\Sigma^+) + h\nu$.
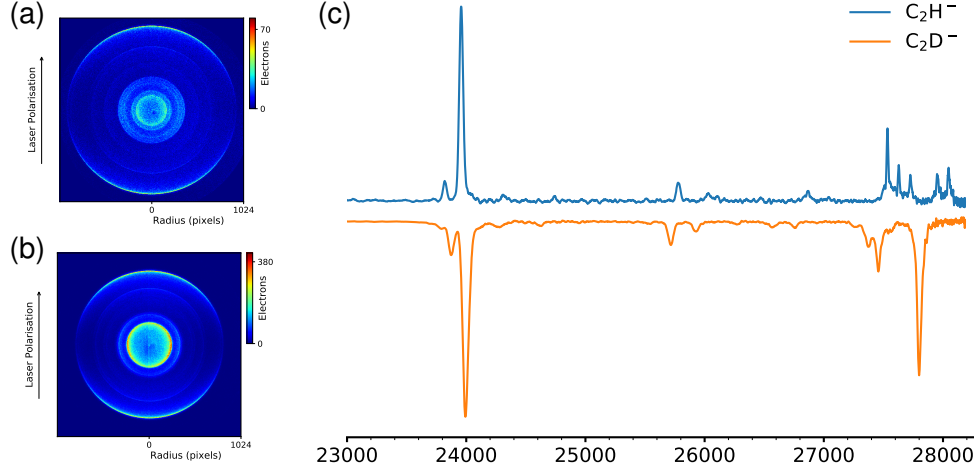

Figure 1: (a) A 3D-representation of the velocity-map image of ~ 4 million photoelectrons detached from C2H$^-$ at 355 nm. The outer rings, distributed around the vertical laser polarisation axis, represents photodetachment to the ground $\tilde{X}\,^2\Sigma^+$ state. The inner rings reprsent detachment to the first excited state $\tilde{A}\,^2\Pi$. (b) Photoelectron spectra of C_2H^- at a range of detachment wavelengths, illustrating the change in electron intensity profile and energy resolution.

To investigate the vibronic coupling interaction between these two nearby Σ^+ and Π surfaces, deuterated ethynyl C_2D^- was also studied. C_2D^- ions were produced in a discharge of pure C_2D_4 gas and measured under the same experimental conditions as C_2H^-. An illustrative VMI of photodetachment at 355 nm from C_2D^- is shown in Fig. 1(b). Similarly to Fig 1(a) two electronic transitions are observed. While the fast electrons appear similar in both images, a striking difference is observed in the slow electrons near the detector center. In Fig. 1(a) a series of weak rings are observed, however in Fig. 1(b) two dominant rings are seen.

The VMIs in Fig. 1 were inverted using the Abel inversion methods detailed in pyAbel, to

extract the corresponding photoelectron spectra presented in Fig. 1(c). Below $27,000$ cm^{-1} on the $\tilde{X}^2\Sigma^+$ surface the C_2H^- and C_2D^- spectra are very similar. Both are dominated by the origin transition, shifted by ~ 10 cm^{-1} in the deuterated spectrum, with progressions involving the v$_2(\pi)$ bending and v$_3(\sigma)$ CC stretch vibrational normal modes. This includes transitions involving an odd quanta of v$_2$ bending excitation (2^{n+1}) which should be totally forbidden within the harmonic oscillator approximation. However, the presence of these transitions in the spectra is likely an indicator of Herzberg-Teller (HT) vibronic coupling between the ground $^2\Sigma^+$ and nearby excited $^2\Pi$ electronic surfaces, as

$$\Sigma^+ \otimes \pi = \Pi. \tag{3}$$

Above $27,000$ cm^{-1}, near the $\tilde{A}^2\Pi$ state origin, large differences are observed between the C_2H^- and C_2D^- photoelectron spectra. In the C_2H^- spectrum 5 sharp peaks are observed, spaced by ~ 95 cm^{-1}. However in the deuterated spectrum, one dominant peak is observed at $27,792$ cm^{-1}, with 3 weaker peaks centred around $27,360$ cm^{-1}. Unlike the structure below $27,000$ cm^{-1} none of these peaks are able to be readily assigned to vibronic transitions, due to the presence of strong coupling interactions between the nearby Σ^+ and Π surfaces.

Vibronic Coupling Interactions

The complex spectral structure observed near the $\tilde{A}^2\Pi$ state origin in Fig. 1(c) may be understood by considering the v_2 bending vibrational mode. To account for the degeneracy of this mode, the vibronic quantum number ℓ_i may be introduced, representing the angular momentum associated with the bending motion. This may take a value of $\ell_i = v_i, v_i - 2, v_i - 4, \ldots, 1$ or 0, where v_i is the quanta of bending excitation. In the Born-Oppenheimer approximation different vibronic energy levels ℓ_i are degenerate, however in cases with strong rovibronic coupling, this degeneracy in ℓ_i is lost.

In C_2H this effect creates a Renner-Teller (RT) pair in the excited state, where the usually

degenerate Π surfaces separate to form two non-degenerate electronic states $\Pi^+(2A')$ and $\Pi^-(1A'')$. This involves separating a single potential energy surface (V) into two distinct but connected surfaces (V$^+$) and (V$^-$). Due to the strong coupling along the linear axis between the electronic and vibration angular momenta of the $2A'$ and $1A''$ components of the $^2\Pi$ state, stationary states cannot be explicitly assigned to either of the $\Pi^+(2A')$ or $\Pi^-(1A'')$ electronic surfaces. Instead, they exist as a combination of both states.

Due to the close lying nature of the ground $\tilde{X}^2\Sigma^+$ and excited $\tilde{A}^2\Pi$ electronic states, which are only separated by ~ 3700 cm^{-1}, a pseudo Jahn-Teller effect is also observed. In the case of C$_2$H this is seen as coupling between the ground $\Sigma^+(1A')$ and excited $\Pi^+(2A')$ states, induced by the bending motion of v_2. The ground state only couples to one of the Renner-Teller pair $\Pi^+(2A')$, as the other state $\Pi^-(1A'')$ has incorrect symmetry. This results in the complex vibronic structure observed for the $\tilde{A}^2\Pi$ electronic state, with contributions from three coupled surfaces $\Sigma^+(1A')$, $\Pi^+(2A')$, and $\Pi^-(1A'')$.

These interactions spread the electronic orgin of the $\tilde{A}\,^2\Pi$ state over several vibronic levels. Therefore, instead of assigning a defined origin, the observed peaks in the spectrum may be assigned to coupled admixtures of vibronic transitions involving the three potential energy surfaces,

$$\Psi_f = \sum_\xi \psi_e^\xi \sum_k C_{fk}^\xi \phi_{fkm}^\xi, \tag{4}$$

where ψ_e^ξ is the diabatic electronic wavefunction, and ϕ_{fkm}^ξ is the spin-rovibrational wavefunction. ξ represents the electronic states used in the expansion ($\xi = \Sigma^+(1A')$, $\Pi^+(2A')$, $\Pi^-(1A'')$). A depiction of these three interacting surfaces is given in Fig. 2.

The adiabatic potential energy surfaces in Figure 2 were calculated using the variational method of Tarroni and Carter. This has been used to calculate a multitude of admixed vibronic levels. In the literature, over 100 possible C$_2$H vibronic states have been calculated, up to 6,400 cm^{-1} above the $\tilde{X}^2\Sigma^+$ origin. However, assigning experimental spectra has remained a challenge, partly due to the large number of calculated levels providing multiple
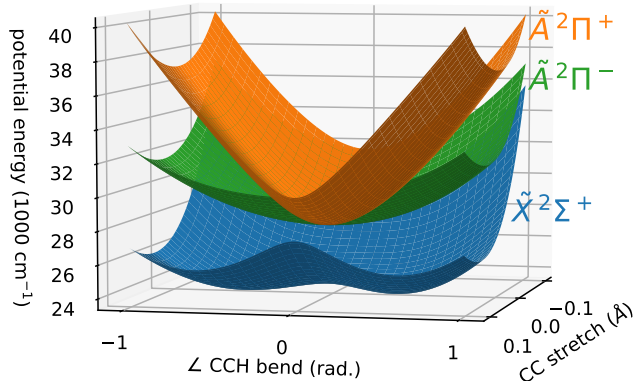
Figure 2: Adiabatic potential energy surfaces of $\tilde{X}^2\Sigma^+$, $\tilde{A}^2\Pi^-$, and $\tilde{A}^2\Pi^+$ states, calculated using the method developed by Tarroni and Carter[?] ($E_{1A'}$, $E_{2A'}$, and $E_{1A''}$ in Eq. 4).

possible assignments for each experimentally observed transition.

Coupling Calculations

In order to guide spectral assignment of C_2H and astronomical searches for other C_nH radicals, transition intensities are also needed. However, due to the strong vibronic coupling interactions, this can not be obtained via standard quantum chemistry methods. To account for these interactions, the photoelectron spectrum of the C_2H^- anion was simulated using a quasidiabatic Hamiltonian of the type advocated by Koeppel, Domcke and Cederbaum (KDC, reference here). In this approach, the Hamiltonian is represented in a basis of quasidiabatic (slowly varying) electronic states for which the kinetic energy operator can be assumed diagonal. For C_2H, the KDC Hamiltonian comprises three states - the two components of the $^2\Pi$ state and the ground $^2\Sigma$ state - and is then projected onto a vibrational basis, usually chosen as a direct product of harmonic oscillators. Diagonalization of the corresponding matrix yields the molecular states (which are given in terms of a Born-Huang expansion), and the squared projections of the corresponding eigenvectors onto the ground state of the anion yield the relative intensities. The latter is automatically true if the photodetachment cross sections for the $^2\Sigma$ and $^2\Pi$ states are assumed equal, but different cross sections of the two states can be incorporated by scaling the intensities of states according

to their (vibronic) symmetry.

Details of the construction and parametrization of KDC Hamiltonians can be found elsewhere in the literature (references), and the procedure followed will be discussed here only briefly. The present calculations use the so-called quadratic vibronic coupling (QVC) model. For the system at hand, the QVC model Hamiltonian assumes the following form

where the summations run over the dimensionless normal modes (q_i) that serve as the coordinate system for the problem. For convenience, the latter are chosen to be those of the anion, which considerably facilitates calculation of the spectral intensities. In Eq. 1, the diagonal terms of V (excluding those that carry the Renner-Teller coupling constant η) represent the quasidiabatic potential energy surfaces of the Σ, and the two components of the Π state, chosen here as those in which the unpaired electron lies within or is perpendicular to an arbitrarily chosen plane, designated as A(a$'$) and A(a$''$), respectively. Δ_0^X is the separation of the anion and Σ states at the origin of the coordinate system (the vertical electron detachment energy), and Δ_0^Π is the gap between anion and Π states at the same geometry.

For the modes of σ symmetry (q_1 and q_3), the diabatic forces (F_i) and force constants (F_{ij}) coincide with those of the adiabatic potential energy surfaces. However, for the bending mode, the diabatic (F_{22}) and adiabatic (f_{22}) force constants differ, and the parametrization is somewhat more involved. For each component of the Π state, either the 2a or 2b component of the bending vibration will maintain the A$'$ electronic symmetry that is needed to couple with the X state. Designating these as 2a for the A(a$'$) state and 2b for the A(a$''$) state (as is implicit in Eq. 1), the diabatic force constants for the bending mode in the X and A states can be written as

where the Renner-Teller interaction strength (η) is determined from

once the interstate coupling (λ which is calculated analytically in this work, see below) is known.

When the potential in Eq. 1 is diagonalized, the adiabatic states that are used for its

parametrization are precisely recovered through second order in displacement. To parametrize this Hamiltonian, the equation-of-motion coupled-cluster method known as EOMIP-CCSDT has been used âĂę (Zach goes from here)âĂę

$$
V = \begin{array}{c} \\ X \\ A(a') \\ A(a'') \end{array} \begin{array}{c} X \\ \left(\begin{array}{c} \Delta_0^X + F_1^X q_1 + F_3^X q_3 + \frac{1}{2}\Sigma_{ij}F_{ij}^X q_i q_j \\ 1 \\ 0 \end{array} \right. \end{array} \begin{array}{c} A(a') \\ 0 \\ \Delta_0^A + F_1^A q_1 + F_3^A q_3 + \frac{1}{2}\sum_{ij}F_{ij}^A q_i q_j + \frac{1}{2}\eta(q_{3a}^2 - q_{3b}^2) \\ 1 \end{array} \begin{array}{c} A(c \\ 1 \\ 0 \\ 0 \end{array}
$$

$$(5)$$

Simulated Spectra

The above method was employed to simulate the photoelectron spectrum of C_2H^-, with the calculated transitions shown in Figure 3(a) alongside the experimental data at 355 nm. On the $\tilde{X}^2\Sigma^+$ surface, below 3,600 cm^{-1}, there is excellent agreement in both the transition positions and intensities between the simulated and experimental spectra. This includes the HT coupled (2^{n+1}) transitions with Π symmetry, which would normally be missing from a simulation using standard *ab-initio* approaches.

The positions of the calculated levels for the $\tilde{A}^2\Pi$ state have been shifted by 1,220 cm^{-1} to account for the EOMIP-CCSDT calculations overestimating the effective Term energy. The experimental data shows that the electronic coupling interactions induce a splitting of the $\tilde{A}^2\Pi$ state origin over 5 vibronic levels, spaced by ~ 95 cm^{-1} (a-e). This splitting is also observed in the calculated spectrum, which correctly predicts 5 prominent transitions in this region. The relative intensities between the calculated transitions are also in good agreement with the experimental data. Peak d is slightly underestimated, however the relative intensity difference between peaks d and e may be partly explained by the Wigner threshold law, which will reduce the intensity of peak e in the experimental spectrum as it is close to the detachment threshold. The simulated spectrum also slightly underestimates

the splitting between the vibronic levels, which may be linked to the overestimation of the gap between the $^2\Sigma$ and $^2\Pi$ surfaces.
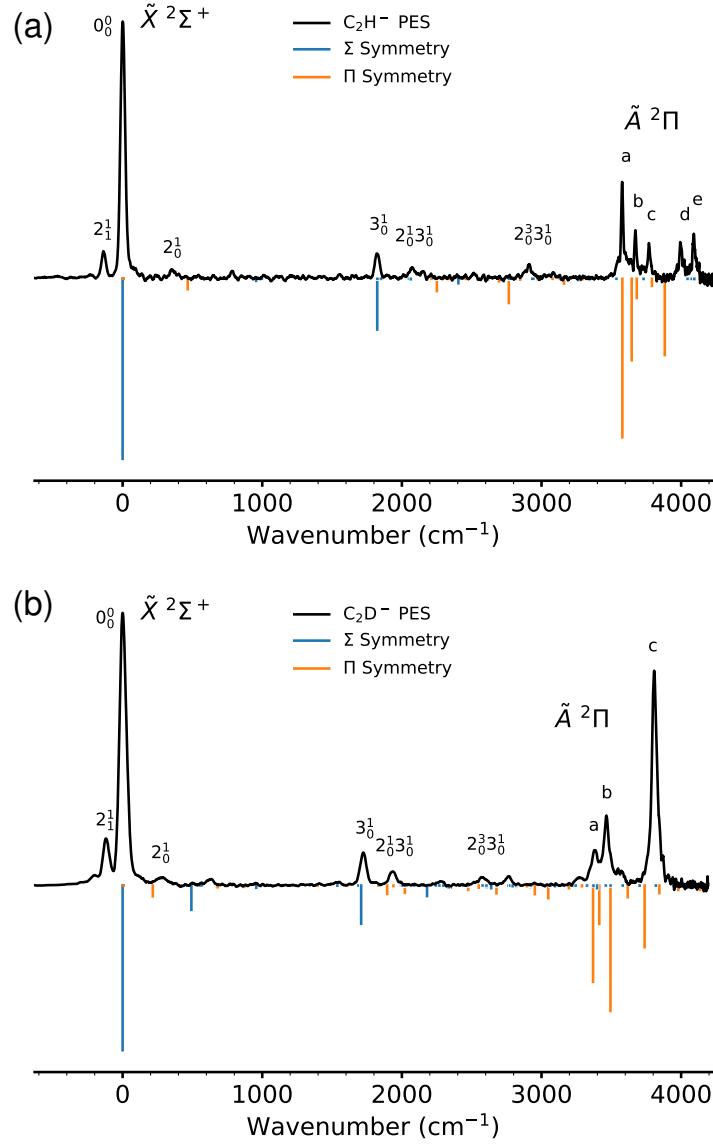

Figure 3: cat

The photoelectron spectrum of C_2D^- was also examined using the same approach, with the calculated transitions shown in Figure 3(b) alongside the 355 nm experimental data. Again, there is excellent agreement in the intensity and calculated positions of the transitions on the $\tilde{X}^2\Sigma^+$ state surface, including the HT coupled levels. Near the $\tilde{A}^2\Pi$ state origin, deuteration has a large impact on the experimental photoelectron spectrum. Instead of

the 5 evenly split levels observed in C_2H, a single dominant peak (d) is now observed at 3,844 cm^{-1} alongside a collection of weaker peaks (a-c) centred around 3,400 cm^{-1}. Based on previous spin-orbit splitting measurements, peak d is expected to have significant $\tilde{A}^2\Pi$ character, with peaks a-c commonly assigned to vibronic levels with predominantly HT coupled $\tilde{X}^2\Sigma^+$ character. This suggests that deuteration effectively dampens the coupling interaction between the surfaces.

Like the experimental spectra, a large change is observed in the simulated spectrum upon deuteration. The calculated intensity pattern of the vibronic levels around the $\tilde{A}^2\Pi$ origin is a good match to the experimental data, with a single intense transition observed near peak d, and 3 prominent transitions predicted around the experimental peaks a-c. The calculated splitting between the levels is also similar, however the relative intensity of peak d appears to be slightly underestimated.
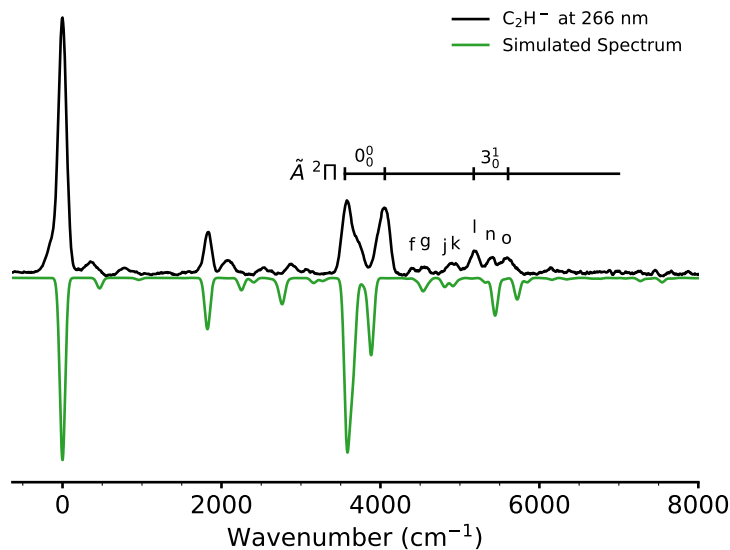

Figure 4: cat

To investigate the effects of coupling on the higher excited vibronic levels on the $\tilde{A}^2\Pi$ surface, the calculations were compared to the experimental photoelectron spectrum of C_2H^- at 266 nm, as presented in Figure 4. Gaussians were fitted to the transitions from Figure 3(a) with a FWHM of 40 cm^{-1} to match the resolution of the experimental data above threshold.

Near 3,900 cm^{-1} the electronic origin of the $\tilde{A}^2\Pi$ state is split over 5 vibronic levels, as discussed above. A similar effect is also observed for the 3_0^1 band, which becomes split over 3 vibronic levels labelled l, n, and o. The calculated spectrum correctly predicts the position and intensity of peaks n and o, but appears to strongly underestimate the intensity of peak l. Between the 0_0^0 and 3_0^1 bands a collection of weaker peaks are also observed (f,g,j,k). These are assigned to highly excited HT coupled $\tilde{X}^2\Sigma^+$ transitions (j,k), and pure $\tilde{X}^2\Sigma^+$ transitions (f,g). Consequently, peaks f and g will possess Σ symmetry, and should have a different anisotropy to all of the other dominant transitions above 3,800 cm^{-1}. The position and intensity of these highly-excited coupled transitions are well described by the simulated spectrum.

The results from Figures 3 and 4 confirm that the quasiadiabtic approach is able to accurately describe the vibronic interactions between the Σ and Π surfaces, including deuteration effects. This validates the proposed vibronic interactions, and demonstrates how this method can be employed to decode and assign even complex spectra. Applying this approach to similar less-studied systems will produce reliable predictions for the position and intensity of dominant transitions, which will help guide the search for these molecules in laboratory experiments and astronomical observations.

Photoelectron Angular Distributions

Symmetry considerations may be employed to help verify the assignments from the calculations above. The EOMIP-CCSDT calculations determine the symmetry of each transitions, either Σ or Π. Experimentally, this may be compared directly to symmetries obtained from the corresponding photoelectron angular distributions. As the detachment laser is linearly polarized, the angular distribution of the electrons in Fig. 1 may be linked to the symmetry of the detachment orbital. For polarised light, the differential cross section is given by

$$\frac{\mathrm{d}\sigma}{\mathrm{d}\Omega} = \frac{\sigma_{\text{total}}}{4\pi}[1 + \beta P_2(\cos\theta)], \tag{6}$$

13

where θ is the angle between the ejected electron and the (vertical) laser polarization, and P_2 is the second-order Legendre polynomial. The anisotropy parameter β provides a quantitative measure of the angular distribution, and can range from -1 to +2 for a pure parallel and perpendicular transition respectively.** From Eq. (8), β may be determined for each transition in a photoelectron spectrum from the slope of I(θ) vs $P_2(\cos\theta)$.

Through conservation of angular momentum, it can be shown that β may also be expressed in terms of partial waves and dipole matrix elements. Explicitly,

$$\beta_\ell = \frac{[\ell(\ell-1)\chi^2_{\ell,\ell-1} + (\ell+1)(\ell+2)\chi^2_{\ell,\ell+1} - 6\ell(\ell+1)\chi_{\ell,\ell-1}\chi_{\ell,\ell+1}\cos\delta_{\ell+1,\ell-1}]/(2\ell+1)}{\ell\chi^2_{\ell,\ell-1} + (\ell+1)\chi^2_{\ell,\ell+1}}, \quad (7)$$

where ℓ is the electron orbital angular momentum of the parent anion orbital, $\chi_{\ell,\ell\pm1}$ is the radial dipole matrix element for the transition from an orbital ℓ to each of the $\ell\pm1$ partial waves, and $\delta_{\ell+1,\ell-1}$ is the phase shift between the two $(\ell\pm1)$ partial waves.

Photodetachment to the ground state of C_2H^- ($\tilde{X}\,^1\Sigma^+$) involves ejecting an electron from an $s-$like $5\sigma_g$ orbital, whereas detachment to the excited ($\tilde{A}\,^2\Pi$) state occurs from a $p-$like $1\pi_u$ orbital.

Symmetry considerations can be employed to help assign the admixed structure in the experimental photoelectron spectra around the $\tilde{A}^2\Pi$ origin. As the detachment laser is linearly polarized, the angular distribution of the electrons in Fig. 1 may be linked to the symmetry of the detachment orbital. For polarised light, the differential cross section is given by

$$\frac{d\sigma}{d\Omega} = \frac{\sigma_{\text{total}}}{4\pi}[1 + \beta P_2(\cos\theta)], \quad (8)$$

where θ is the angle between the ejected electron and the (vertical) laser polarization, and P_2 is the second-order Legendre polynomial. The anisotropy parameter β provides a quantitative measure of the angular distribution, and can range from -1 to +2 for a pure parallel and perpendicular transition respectively.** From Eq. (8), β may be determined for each transition in a photoelectron spectrum from the slope of I(θ) vs $P_2(\cos\theta)$. Through con-

servation of angular momentum, it can be shown that β may also be expressed in terms of partial waves and dipole matrix elements. Explicitly,

$$\beta_\ell = \frac{[\ell(\ell-1)\chi^2_{\ell,\ell-1} + (\ell+1)(\ell+2)\chi^2_{\ell,\ell+1} - 6\ell(\ell+1)\chi_{\ell,\ell-1}\chi_{\ell,\ell+1}\cos\delta_{\ell+1,\ell-1}]/(2\ell+1)}{\ell\chi^2_{\ell,\ell-1} + (\ell+1)\chi^2_{\ell,\ell+1}}, \quad (9)$$

where ℓ is the electron orbital angular momentum of the parent anion orbital, $\chi_{\ell,\ell\pm1}$ is the radial dipole matrix element for the transition from an orbital ℓ to each of the $\ell\pm1$ partial waves, and $\delta_{\ell+1,\ell-1}$ is the phase shift between the two $(\ell\pm1)$ partial waves.

As the radial dipole matrix elements will vary with electron kinetic energy, so too will β. Therefore, measuring anisotropy parameters at a range of energies will reveal the character of the detachment orbital. Anisotropy parameters were calculated for all resolved transitions in the C_2H^- photoelectron spectra from $266 - 355$ nm, as shown in Fig. ??.

Photodetachment to the ground state of C_2H^- $(\tilde{X}\,^1\Sigma^+)$ involves ejecting an electron from an $s-$like $5\sigma_g$ orbital, whereas detachment to the excited $(\tilde{A}\,^2\Pi)$ state occurs from a $p-$like $1\pi_u$ orbital. For a pure s and p orbital, the energy dependence of the anisotropy parameter may be described by Equations (10) and (11) respectively,

$$\beta_s = 2, \quad (10)$$

and,

$$\beta_p = \frac{2A_1^2\epsilon^2 - 4A_1\epsilon\cos\delta_{2,0}}{1 + 2A_1^2\epsilon^2}, \quad (11)$$

where the Hanstorp coefficient A_1 relates to the ratio of radial matrix elements $\frac{\chi_{1,2}}{\chi_{1,0}}$ and $\delta_{2,0}$ represents the partial wave phase shift. As molecular orbitals may not be pure, we can describe the detachment from C_2H^- using the mixed sp model of Sanov,[3]

$$\beta(\epsilon)_{sp} = \frac{2Z\epsilon + 2A_1\epsilon^2 - 4\epsilon\cos\delta_{\ell\pm1}}{\frac{1}{A_1} + 2A_1\epsilon^2 + Z\epsilon} \quad (12)$$

where f is the percentage of p character of the orbital,

$$Z = \frac{1-f}{f}\frac{8}{3} \text{ and } |\psi\rangle = \sqrt{1-f}|s\rangle + \sqrt{f}|p\rangle. \tag{13}$$

Therefore, calculating the anisotropy parameter for a given transition will reveal the symmetry of the state, which can be compared to the symmetry of the calculated vibronic levels. However this is complicated by the presence of HT coupling, which allows for the electronic character of two surfaces to be mixed via a vibrational promoting mode. As shown in the Supplementary Materials, the transition dipole moment for a HT coupled transition may be rewritten as

$$\mu_\alpha^{a-n} = \langle \Psi_{\text{anion}} | \vec{\mu_\alpha} | \Psi_{\text{neutral}} \rangle \tag{14}$$

$$= \mu_{\alpha:0}^{\tilde{X}-\tilde{X}} \langle \chi''_{ms} | \chi'_{jt} \rangle + \gamma_{kr,jt} \mu_{a:0}^{\tilde{A}-\tilde{X}} \langle \chi''_{ms} | Q_n | \chi'_{kr} \rangle \tag{15}$$

where $\mu_{\alpha:0}^{\tilde{X}-\tilde{X}}$ and $\mu_{a:0}^{\tilde{A}-\tilde{X}}$ are the electronic transition moments for the $\tilde{X} \leftarrow \tilde{X}$ and $\tilde{A} \leftarrow \tilde{X}$ transitions, χ''_{ms}, χ'_{jt}, and χ'_{kr} are the nuclear components of the anion and neutral respectively, and $\gamma_{kr,jt}$ is the vibronic coupling constant. Therefore, HT coupled transitions on the $\tilde{X}^2\Sigma^+$ surface are expected to have anisotropy parameters that reflect the coupled $\tilde{A}^2\Pi$ surface.

Anisotropy parameters were calculated for all strong transitions in the C_2H^- photoelectron spectra from $355 - 266$ nm, as shown in Fig. **??**.

HT coupling allows for the electronic character of two surfaces to be mixed via a vibrational promoting mode. As shown in the Supplementary Materials, the transition dipole moment for a HT coupled transition may be rewritten as

$$\mu_\alpha^{a-n} = \langle \Psi_{\text{anion}} | \vec{\mu_\alpha} | \Psi_{\text{neutral}} \rangle \tag{16}$$

$$= \mu_{\alpha:0}^{\tilde{X}-\tilde{X}} \langle \chi''_{ms} | \chi'_{jt} \rangle + \gamma_{kr,jt} \mu_{a:0}^{\tilde{A}-\tilde{X}} \langle \chi''_{ms} | Q_n | \chi'_{kr} \rangle \tag{17}$$

where $\mu_{\alpha:0}^{\tilde{X}-\tilde{X}}$ and $\mu_{a:0}^{\tilde{A}-\tilde{X}}$ are the electronic transition moments for the $\tilde{X} \leftarrow \tilde{X}$ and $\tilde{A} \leftarrow \tilde{X}$ transitions, χ''_{ms}, χ'_{jt}, and χ'_{kr} are the nuclear components of the anion and neutral respectively, and $\gamma_{kr,jt}$ is the vibronic coupling constant. By comparing Eq. (17) to a Taylor series expansion of the transition dipole moment in Q_n about the anion equilibrium geometry, one can see that the vibronic coupling constant may be defined as,

$$\left(\frac{\partial \mu_\alpha^{\tilde{X}-\tilde{X}}}{\partial Q_n} \right)_0 = \gamma_{kr,jt} \mu_{a:0}^{\tilde{A}-\tilde{X}}. \tag{18}$$

Equation (18) shows that information about the vibronic coupling interaction between the neutral $\tilde{A} - \tilde{X}$ states may be obtained from determining the slope of the $\tilde{X} - \tilde{X}$ electronic transition moment along the vibrational promoting mode coordinate Q_n.

The resolution attainable using velocity-map imaging is dependent on the energy of the photoelectrons, $\Delta\epsilon \propto \epsilon$. Therefore, measurements close to threshold will provide the highest energy resolution, while shorter wavelength measurements will map a greater extent of the neutral vibrational structure. This variation is illustrated in Fig. 1(b), which shows the photoelectron spectra of C_2H^- resulting from photodetachment at 266 nm, 300 nm, 310 nm, 320 nm, and 355 nm. In the shorter wavelength measurements, spectral structure related to the $\tilde{A}\,^2\Pi$ state is observed up to 6000 cm^{-1} above the $\tilde{A}$ sate origin. A high resolution photoelectron spectrum of C_2H^- detachment at 355 nm extracted from a 2048×2048 image, similar to Fig. 1(a), via an inverse Abel transformation, is shown in Fig. **??**

Conclusions

Methods

Details of the HR-PEI spectrometer are given in Refs 4 and 5. CH_2CN^- ions are produced by passing a 1:1 C_2H_4:N_2O gas mixture through a pulse valve, which then undergoes supersonic expansion into a high-voltage discharge. Negative ions are extracted, accelerated to 500 eV,

and focussed into a novel gating, bunching, and re-referencing unit.[6] Anions are mass separated over a 2m time-of-flight region, with the ion of interest isolated by an electrostatic gate. The ion packet is crossed with a tuneable detachment laser beam, generated from a Sunlite EX optical parametric oscillator pumped by the third harmonic of a Continuum Powerlite 9010 Nd:YAG laser. The laser produces between 10-50mJ per pulse at 10Hz, depending on whether the idler or signal beam is used. The wavelength of the laser light is measured using a HighFinesse WS7 UV wavemeter.

A velocity-map imaging lens, a modified version of the original concept of Eppink and Parker, images the detached electrons to a 75mm diameter MCP/phosphor screen detector. Events are imaged by a 2014x2048 monochrome CCD camera (PCO 2000), with each frame transferred to a computer at a 10Hz repetition rate, and processed in real time to identify individual electron events. The electron positions are centroided to a sub-pixel accuracy, then written to a data file for subsequent analysis. The velocity-map image is centred and then circularized by an angular dependent-radial scaling determined by comparing adjacent radial slice intensity profiles.[7] An inverse Abel transformation of the VMI, based on the algorithm of Hansen and Law,[8,9] returns a slice image of the 3D electron source distribution. Absolute energy calibration of the photoelectron spectra is achieved using published measurements of species, including O^- [4] and NO_2^-,[?] that have been studied under similar conditions as used for the CH_2CN^- measurements.

In standard operation, the energy distribution of the detached electrons is obtained by recording the velocity-mapped positions from photodetachment at a fixed wavelength. However the HR-PEI spectrometer may also be reconfigured into an electron counting mode, where the number of events per laser shot is recorded, while the detachment laser wavelength is varied.

Acknowledgement

References

(1) Ervin, K. M.; Lineberger, W. C. Photoelectron spectra of dicarbon(1-) and ethynyl(1-). *The Journal of Physical Chemistry* **1991**, *95*, 1167–1177.

(2) Jahn, H. A.; Teller, E. Stability of polyatomic molecules in degenerate electronic states - I Orbital degeneracy. *Proceedings of the Royal Society of London A: Mathematical, Physical and Engineering Sciences* **1937**, *161*, 220–235.

(3) Sanov, A. Laboratory-Frame Photoelectron Angular Distributions in Anion Photodetachment: Insight into Electronic Structure and Intermolecular Interactions. *Annual Review of Physical Chemistry* **2014**, *65*, 341–363.

(4) Cavanagh, S. J.; Gibson, S. T.; Gale, M. N.; Dedman, C. J.; Roberts, E. H.; Lewis, B. R. High resolution velocity-map imaging photoelectron spectroscopy of the O^- fine-structure transitions. *Physical Review A* **2007**, *76*, 052708.

(5) DeVine, J. A.; Weichman, M. L.; Laws, B.; Chang, J.; Babin, M. C.; Balerdi, G.; Xie, C.; Malbon, C. L.; Lineberger, W. C.; Yarkony, D. R. et al. Encoding of vinylidene isomerization in its anion photoelectron spectrum. *Science* **2017**, *358*, 336–339.

(6) Dedman, C. J.; Roberts, E. H.; Gibson, S. T.; Lewis, B. R. Fast 1 kV metal-oxide-semiconductor field-effect transistor switch. *Review of Scientific Instruments* **2001**, *72*, 3718–3720.

(7) Gascooke, J. R.; Gibson, S. T.; Lawrance, W. D. A âĂIJcircularisationâĂİ method to

repair deformations and determine the centre of velocity map images. *The Journal of Chemical Physics* **2017**, *147*, 013924.

(8) Hansen, E. W.; Law, P.-L. Recursive methods for computing the Abel transform and its inverse. *Journal of the Optical Society of America A* **1985**, *2*, 510–520.

(9) Hickstein, D. D.; Yurchak, R.; Das, D.; Shih, C.-Y.; Gibson, S. T. PyAbel (v0.7): A Python package for Abel transforms. https://github.com/PyAbel/PyAbel, 2016.